DOI: 10.13009/EUCASS2023-844
Aerospace Europe Conference 2023 – 10TH EUCASS – 9TH CEAS

Low cycle fatigue and creep properties of a new L-PBF additive manufacturing copper-maraging steel metal matrix composite for liquid rocket engine thrust chambers

Matteo Crachi[⋆•], *Raffaella Sesana*[⋆], *Cristiana Delprete*[⋆], *Marco Pizzarelli*[◦], *Domenico Borrelli*[⋆†] *and Nicola Sicignano*[⋆†]
[⋆] *DIMEAS, Department of Mechanical and Aerospace Engineering, Politecnico di Torino University*
Corso Duca degli Abruzzi 24, 10129 Torino, Italy
[◦] *Italian Space Agency (ASI),*
Via del Politecnico, 00133 Roma, Italy
[⋆] *Sophia High Tech S.r.l.*
Via Malatesta 30 A, 80049 Somma Vesuviana, Italy
matteo.crachi@polito.it · raffaella.sesana@polito.it
[•]Corresponding author

Abstract

Liquid rocket engine regenerative thrust chambers are a critical component of launch vehicles. Since the material behavior with respect to the temperature drives the stress-strain plastic behavior of the aforementioned hardware, it is of primary importance to select an adequate compromise between thermal conductivity and mechanical properties. In the present study an innovative metal matrix composite, processed by LPBF additive manufacturing, is proposed. Nowadays, the so called dog house cycling failure mechanism of thrust chambers is still under investigation by the scientific community since it is driven by multiple material behaviors: low cycle fatigue, creep end local plastic instability. The present work aims to present the high temperature low cycle fatigue and creep properties investigated by an experimental activity performed on the new copper-maraging steel alloy.

1. Introduction

Thrust chamber of high performance bi-propellant liquid rocket engines is a critical component of the launch vehicles because it is designed to operate in some of the most severe conditions seen in engineering practice. The requirement of reducing the temperature of the walls exposed to the hot gases can be met with high-thermal conductivity copper alloys while the mechanical stiffness is achieved by using high strength steel or nickel alloys. Because the stress-strain behaviour of a regeneratively cooled thrust chamber is directly correlated with its temperature behaviour, it is of primary importance to select the correct alloy.

Regenerative cooling is the most prevalent cooling mechanism in large liquid rocket engines. One or both of the propellants used in the rocket engine are pumped into suitable cooling channels that constitute the combustion chamber or nozzle. The heated coolant is then injected into the combustion chamber, resulting in more efficient combustion, due to the increased initial energy content of the propellant prior to injection (Figure 1(a)).

A material with excellent thermal conductivity, together with a thin wall hardware design, will reduce thermal strains in regeneratively cooled thrust chambers with high performance and high heat transfer. Extended surfaces, known as fins or ribs (Figure 1(b)), can be used to reduce the wall temperature on the hot side of the cooling channels in a regeneratively cooled combustion chamber by increasing the coolant side surface area compared to the hot-gas side surface.

1.1 Regenerative cooling systems fracture mechanism

The demand for high performance and re-usability rocket engines has created major design challenge. One of the critical aspects of the design of combustion chambers is the fatigue life analysis. This has become a major design problem since a portion of the chamber, particularly the throat section, is subjected to cyclic plastic strain due to the high temperature differential between the hot inner wall and the relatively cool outer wall (outer shell) during the engine

Copyright © 2023 by First Author. Posted on line by the EUCASS association with permission.

DOI: 10.13009/EUCASS2023-844

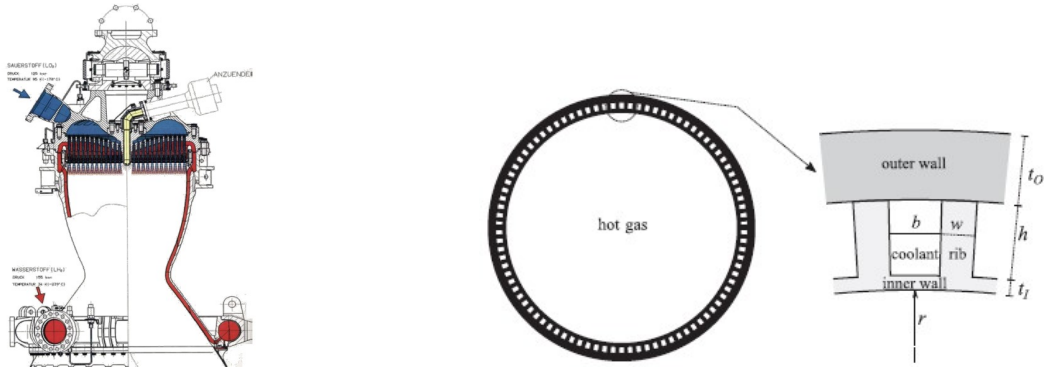

((a)) ((b))

Figure 1: a) Schematic representation of the Vulcan thrust chamber assembly system.[6] b) Schematic of a regenerative thrust chamber cross section[15]

start-stop transients as well as during steady state operation. This has a major impact on nozzle life and creates the need to accurately predict when an engine may fail.

Common strategies aims to contain the high chamber pressure and transmit thrust load using a nickel-alloy closeout jacket. To disperse heat more efficiently, a higher conductive material is utilized for the inner wall, sacrificing strength and resistance. This difference between inner and close out wall material is reflected to different thermal expansion properties. In addiction, the different thickness of the inner wall respect to the close out wall leads to very different thermo-structural behaviour: the inner wall, more conductive, designed in order to have low thickness compared to the close out wall and with a high thermal dilatation, can rapidly achieve a major volume respect to the close out which has a higher resistance but a low thermal conduction and a lower thermal dilatation. The outer wall constrains the inner wall through the ribs. In particular when the inner wall is hotter than the outer wall during engine start-up and continuous firing, compressive plastic strains of the order of a few percent (up to 3%) are induced in the inner wall as the hot inner wall tends to expand but is restricted by the cold outer wall. On the other side, when the engine is shut down, the inner wall cools down faster than the outer wall, causing tensile plastic strains in the inner wall (Figure 2(a) and Figure 2(b)). The largest and minimum temperature discrepancies occurs during the start-up and shut-down transient phases.

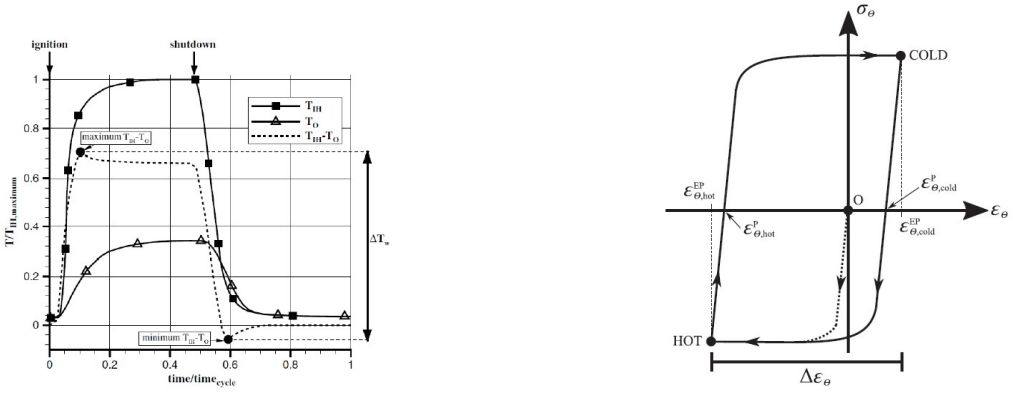

((a)) ((b))

Figure 2: a) Typical behavior of the hot-gas-side (T_{IH}, squared dots) and backside wall temperatures (T_o, triangular dots) and their difference for a regeneratively cooled thrust chamber (dotted line).[15] b) Common cyclic stress-strain behavior of the hot-gas-side wall for a regeneratively cooled thrust chamber[15]

When the engine is fired repeatedly, the plastic deformations in the inner wall accumulate cyclically. For this reason the thrust chamber life is determined by low cycle fatigue and creep behaviors. The consequent strain range $\Delta\varepsilon_{total}$ accumulated in a duty cycle has a significant impact on thrust chamber life since, the larger the strain range is, the shorter the cyclic life. If the strain range is roughly estimated as $\Delta\varepsilon = 2\alpha\Delta T_{totalrange}$ it is possible to state that the higher the difference between inner and close out wall temperature, the lower the engine life.[16] The main combustion

DOI: 10.13009/EUCASS2023-844

chamber (MCC) of the Space Shuttle Main Engine (SSME) is a typical state-of-the-art regeneratively cooled thrust chamber. The hot-gas-side wall is nominally at 867 K during steady-state operation in the most thermally solicited portion near the engine throat, and the resultant heat flux is 160 $\frac{MW}{m^2}$, whereas the outside wall is at 172 K. The whole structure reaches roughly 33 K before and after the engine start and shut-down. Furthermore, the internal pressure of the coolant hydrogen in the throat region during engine firing is 434 bar, which is roughly 300 bar higher than the hotgas pressure of 145 bar.[3] This is a clear example of the harsh thermomechanical environment in which a high-performance liquid rocket engine's thrust chamber operates.

1.2 Thermally induced deformations of regenerative thrust chambers

In regenerative thrust chmabers the main fracture mechanism is related to thermal induced deformation of the cooling channels. Therefore, the main load to face is not the pressure difference between hot gases and cooling system, but the temperature difference of cooling channels. The estimated strain range value, assuming a nominal and fixed chamber geometry, is used in conjunction with results from uniaxial, isothermal fatigue tests performed in a laboratory to determine chamber life. Typically, this method fails because the chamber material degrades sooner than intended. Nowadays, the methodology to be used in order to better estimate the life of a liquid rocket engine is still under development. A modern approach is to use the so called Themo-Mechanical-Fatigue (TMF) panels to validate the numerical analysis and material behavior and then use the validated code to analyse the real engine nozzle geometry,[17],[12].[21] The SSME-MCC is a good illustration of how the engine's actual life has reduced its reusability and, as a result, increased its ongoing cost. In fact, the expected life was reduced to 50 missions[16] from an earlier aim of 100 missions with an overall run duration of around 8 hours[2] due to inappropriate life design and prediction criteria (Figure 3(a)). After experiencing a different life behavior than planned, the main injector's design was updated to include film cooling to protect the chamber wall from overheating.[3] In practice, none of the 46 SSMEs constructed has flown more than 20 times (on average nine times), and the SSME-MCC liners have been polished to minimize hot-gas-side roughened areas as a result of the effect of degradation of the inner wall finishing.[9]

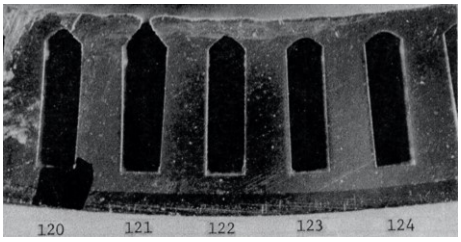

((a))

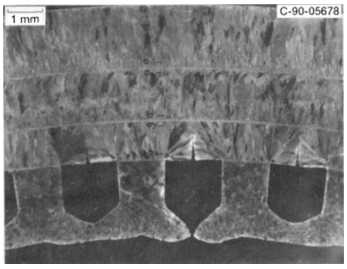

((b))

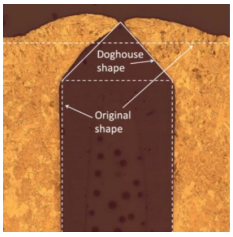

((c))

Figure 3: a) Throat section of SSME - MCC showing channel rupture.[3] b) Typical thrust chamber tested at NASA in the 1970s.[14] c) Standard 'Dog House' fatigue failure in OFHC copper liner[7]

In general, experimental data reveal that as the cycles accumulate, the inner wall thins and bulges incrementally throughout the heating and cooling cycles associated with each firing, eventually failing.[16] As a result, channel wall thinning is the most important element in determining how long regeneratively cooled thrust chambers may be reused. The analysis and comprehension of such phenomena is further complicated by the fact that a detailed analysis of the failure site reveals that roughening of the hot-gas side wall may occur,[16] that the hot-gas wall surface may be subjected to oxidation (i.e., the blanching effects[9]), and that a rupture may occur via low-cycle fatigue (crack rupture) or plastic instability (tensile ductile rupture), depending primarily on the time-dependent behavior of the material. Figure 3(b) shows a detailed shot of a typical failure site of a cyclically fired thrust chamber tested at NASA in the 1970s.[14] This phenomenon is known as the 'dog house effect' because of the shape of such a deformed building. Another clear example is presented in Figure 3(c).[7] The thinning and bulging of the inner wall can be seen clearly at these types of failure locations. The considerable, thermally induced plastic strains that develop in the hot-gas-side wall during cyclic firing, as well as the biasing coolant-to-hot-gas pressure differential across the wall, are related to the deformation of the inner wall.[16] It is important to remark that, because compressive stress cannot generate the cracks seen in the studies (Figure 3(b) and 3(c)), the chambers normally do not break during engine firing, but rather during shut down of the cycle, when walls are subkected to tensile stresses during the shout down transient phase.

DOI: 10.13009/EUCASS2023-844

2. Materials and method

The Metal-Matrix-Composite material is composed by two different powders mixed before the additive manufacturing process: 65% in weight fraction of pure copper and 35% in weight fraction of 17 4PH maraging stainless steel. This study provide a preliminary micrography, high temperature isotherm low cycle fatigue and creep characterization of the material in order to investigate the feasibility of using the material for a future re-usable rocket engine design.

Legor Powmet, supplier of the pure copper (PM-CU101P©) gas atomized powder, provide a particles size analysis which consist in D10=5μm, D50=10μm and D90=17μm.The nominal size declared range is 5-25μm. On the other hand Carpenter Additive 17 4PH powder supplier provide the minimum and maximum size of the powder, thus respectively 15 μm and 45 μm.

In order to mix the two aforementioned different powders, the innovative POWMIX additive manufacturing powder mixer machine developed by Sophia High Tech S.r.l. has been used. This technology allows mixing of two or more powder alloys with an inert gas (Figure 4). Because of the possibility of density instability, an acoustic field is used to break all electrostatic forces to ensure a stochastic distribution of the mixed powder composed by the different starting powders on the printing machine platform. Therefore, the technology consists of the dual action of a pressurised gas and a sound pressure field, for both a macroscopic and microscpoic mixing effect.. These actions mix and amalgamate mixtures of metal powders to be used for the production of hardware characterised by a high level of customisation, in terms of both shape and material, using additive technologies such as Cold Spray and Additive Manufacturing.

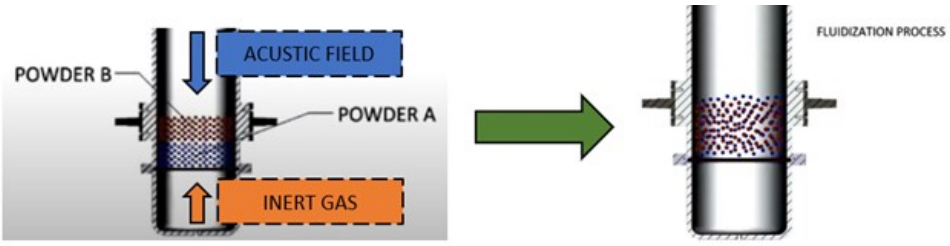

Figure 4: POWMIX powder mixing process logic

The L-PBF additive manufacturing printing machine is a Concept Laser M2 with a working volume of 250mm x 250mm x 250mm and nitrogen gas has been used for processing the metal matrix composite material. Process parameters are presented in Table 1.

Table 1: Cu174PH6535 metal matrix composite additive manufacturing process parameters

	General	Body	Contour
Fusion Strategy	Island (5mm length)		
Layer Thickness t [mm]	0.03		
Hatch Distance h [mm]	0.105		
Spot Size φ [mm]	0.15		
Velocity v [mm/s]		253	400
Power P [W]		200	180
Beam Compensation δ [mm]			0.075
Overleap Factor A1		0.7	

The island scanning strategy has been used in the present study. This strategy divides each layer into smaller islands that are scanned in a random order, keeping the scanning vectors perpendicular to the neighboring islands' scanning vectors. While printing subsequent layers, the islands are shifted with a random ϑ_i angle (Figure 5(a)) in both x and y directions.[10] Moreover, the random algorithm implemented inside the machine controller, does not perform the same printing island order layer by layer: every new powder layer has a random melted island path. The advantages of this strategy can be identified in the ability to shorten the scan vector and reduce residual stress through better cooling dissipation phenomena,[18],[10].[8]

The low cycle fatigue and creep specimen supports have a straight 0.3mm diameter cylindrical shape and are machined after the cut-out activity from the platform is performed with a water-cooled band saw. Cube specimens have been printed on the platform without support. The layout of the additive-manufactured jobs is presented in Figures 5(b)

DOI: 10.13009/EUCASS2023-844

((a)) ((b)) ((c))

Figure 5: Additive Manufacturing scanning strategy and job layout. a) Layer random island strategy. b) Printing Job number 1 with cube specimens for micrography analysis at the top left corner of the platform. c) Printing Job number 2 with low cycle fatigue and creep row cylinders before machining.

and 5(c). Cube specimens have been extracted from Job number 1, that presents different additional geometries, while low cycle fatigue specimens, together with creep specimens, have been printed in Job number 2.

The fracture mechanism of LRE regenerative cooling thrust chambers is a combination of LCF and plastic instability induced by thermal compression-tensile behavior because of the temperature difference during start-up and shut-down operation of the engine. Therefore, the crack opening mechanism (Figure 6(a)) does not appear in the XY plane, but in the z-axisymmetric plane (ZX or ZY plane).Because of the exposed scientific evidence, the present study has analyzed mechanical properties only respect to specimen printed with the axis oriented parallel to the X or Y direction of the machine platform. This choice have been done in order to better replicate the fracture propagation in real hardware operative condition.

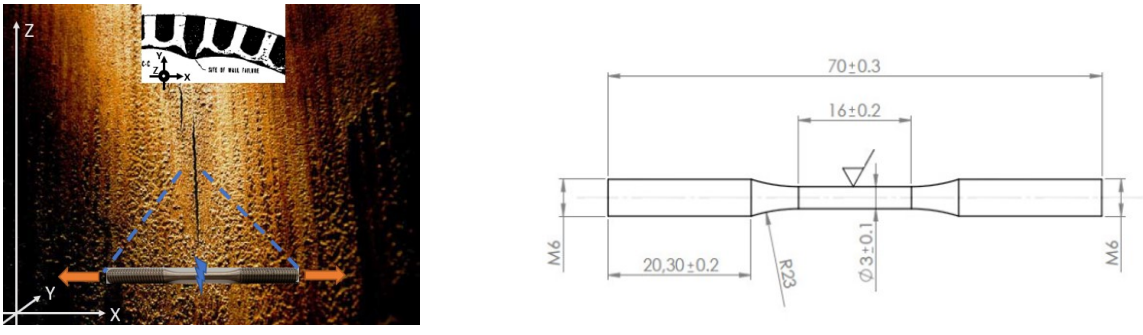

((a)) T ((b))

Figure 6: a) ypical LRE z-axisymmetric plane fracture.[6] b) Low cycle fatigue and creep tests specimen geometry.

The final geometry of low cycle fatigue and creep specimens is represented in Figure 6(b). The printed geometry is identified by a 80mm length cylinder with a 8mm diameter. In order to achieve the specimen shape a machining process has been performed. The specimen's surface morphology has been evaluated with a Veeco Wyko NT1100 Optical Profiling System: surface roughness results to have a $R_a = 2.45$ (Figure 7)

Cube specimens have a paralleled geometry of 20mmx20mmx20mm. Manual polishing was performed with a sander machine (grit size increased from 800 to 4000) and water coolant. The last polishing step has been performed with a synthetic disk cloth and a water based 3 μm diamond suspension. Micrography and fracture surface analysis were performed with a Keyence VHX-7000 microscope.

Low cycle fatigue and creep tests have been performed with a INSTRON Electro-Thermal Mechanical Testing (ETMT). This machine is equipped with a vacuum chamber in order to prevent oxidation during tests by means of argon gas. The strain control is actuated via LVDT. A secondary LVDT is mounted in order to check buckling instability during the test. Both sensors are secured to the grips of the specimen. High temperatures are achieved using the joule effect generated with a high Ampere current through the specimen. The machine is designed to have a PID control loop and moderate the current amperage in order to target the required temperature measured with a spot-welded

DOI: 10.13009/EUCASS2023-844

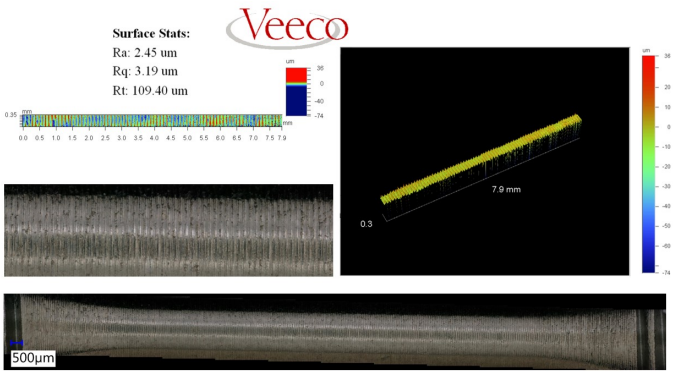

Figure 7: LCF specimen's roughness measurement after machining: 3D profile reconstruction and optical magnification

thermocouple. However, in order to prevent high surface morphology modifications, the temperature control has been actuated using a pre-characterized Ampere-temperature curve with respect to a random specimen of the same material: the temperature has been recorded during current amperage increasing steps. Figure 8 shows the repeatability of the temperature-current curve during characterization tests A and B. Then creep and low cycle fatigue tests have been performed at the constant current amperage magnitude required in order to achieve the target temperature of the test.

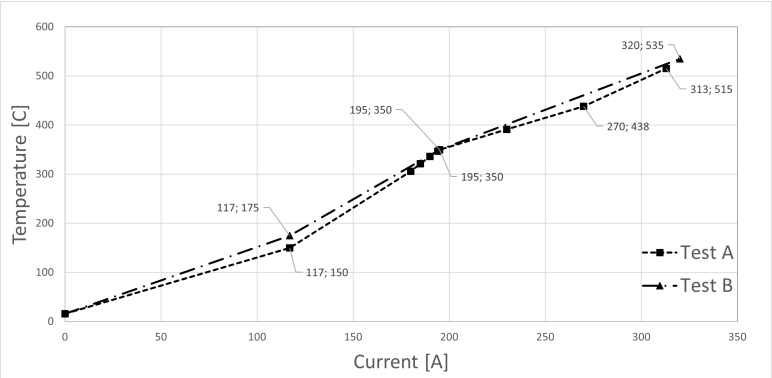

Figure 8: Temperature-current curve during characterization test A and B

The low cycle fatigue tests have been performed at a frequency of 1 Hz by means of sinusoidal shape. A $R_\varepsilon = \frac{\varepsilon_{min}}{\varepsilon_{max}} = -1$ centered strain cycle is applied with respect to all low cycle fatigue tests and 100 points par cycle have been recorded. All tests were carried out until the specimen fractured (except for two room temperature low deformation tests). The target $\varepsilon\%_{eng.tot}$ and temperatures of the tests have been selected in order to be representative of common strains and temperatures of liquid rocket engines. Before starting the test a waiting time of 300 s in load control at 0 N was applied in order to homogenise the temperature of the middle section of the specimen. Table 3 shows a summary of the low cycle fatigue test activity at room and high temperatures. Out of 36 available specimens for low cycle fatigue and creep tests, 32 have been employed for low cycle fatigue analysis. However, due to the complex set-up of the experiment, temperature-current calibration procedure and buckling instability, only two tests out of the 16 presented in Table 2 have been performed more then one time.

The same procedure to target the correct temperature used for low cycle fatigue test has been applied for the creep tests. For the same reason aforementioned, only 3 creep tests have been tested (Table 2). Creep tests have been performed at two different temperatures, 300^{o}C and 500^{o}C for 100 hours. Cu174PH6535 is a new innovative material and therefore the creep behavior was unknown: the main objective of the 300^{o}C test was to have a first trial test in order to better understand the mechanical visco-plastic attitude of the Cu174PH6535. The 300^{o}C test have been performed with a stress load which allowed the material to exhibit at least a plastic deformation. Therefore, by analysing the traction tensile test, a stress of 270 MPa, at 300^{o}C, have been chosen in order to target a 0.5 % total strain and therefore to ensure that the plastic domain was achieved. On the other hand, the 500^{o}C, have been performed due to the more close temperature condition of a common LRE thrust chamber. The same logic was applied for one of the tests at 500Â°C, in order to achieve a 0.5 % total strain, thus a 170 MPa stress has been applied. The second 500^{o}C

DOI: 10.13009/EUCASS2023-844

test has been performed with the purpose of providing a strain rate for a different stress load of 117 MPa at the same temperature, and therefore obtaining a strain rate vs stress trend profile.

Table 2: Low Cycle Fatigue and creep experimental campaign

	LCF tests						Creep tests		
	$\Delta\varepsilon_{tot}\%$						$\sigma[MPa]$		
	0.5	1.0	1.4	2.0	2.8	3.6	117	170	270
T_room	•		•	•	•	•			
T_150^{o}C				•	•	•			
T_300^{o}C									•
T_350^{o}C				•	•	•			
T_500^{o}C							•	•	
T_550^{o}C		•	• •	•	••	•			

3. Results

3.1 Micrography

The Cu174PH6535 custom powder material shows a bi-metalmatrix-composite microstructure. The material has a very high compenetrated bi-material matrix. The two different materials do not create a unique alloy but instead, after the local melting process, the bi-structured composite shows different alloys: pure copper and 17 4PH. The XY planer microstructure shows that the custom mixed powder is homogeneously spread along both the X and Y directions: the powder mixing process is able to achieve a uniform powder distribution. The most interesting and innovative result of this analysis is that the material has two main regions that are independently melted and one well mixed region. The copper matrix: A copper base matrix is clearly visible (orange color) in Figure 9. This is the main structure of the composite material; 17-4PH islands: 17-4PH islands are visible (bright blue) in Figure 9; Dotted matrix: this third particular areas are a high densified mixture of cooper and 17-4PH. However, also in these particular areas, the copper is the base component, without a standard shape, and the 17-4PH is presented with more spherical shapes inside the copper matrix. Furthermore it is possible to clearly identify two different sub-areas: one with a low rate of 17-4PH spherical spots (Figure 9(b)) and a second one with a very high rate of spherical spots (Figure 10(b)). The microstructure of the Cu174PH6535 seems to have a liquid phase separation. This behavior has been tested by Xiaosi Sun et al.[19] and a specific characterization of the solidification process is presented: the experiment reveals that steel, during the liquid-to-solid solidification, tries to decouple from copper.

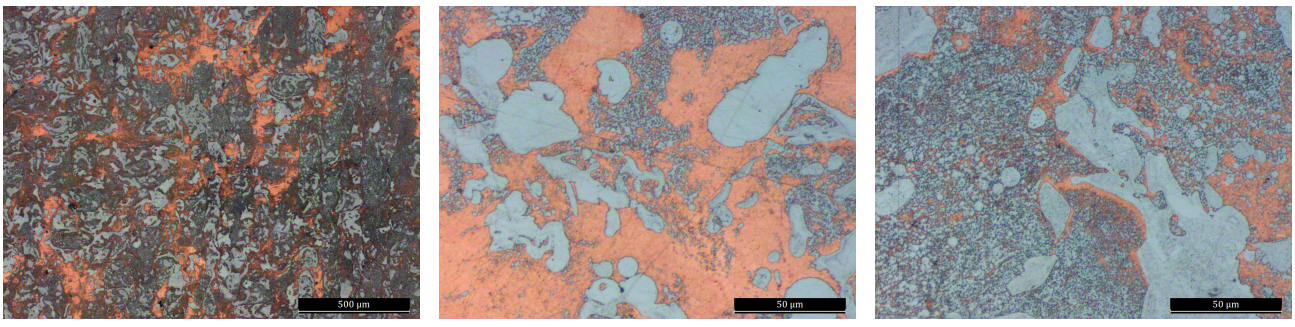

((a)) ((b)) ((c))

Figure 9: Cu174PH XY plane micrography. a) General XY plane microstucture presentation. b) Copper matrix and 174PH island with low rate spherical maraging steel dots. c) Very high rate of spherical maragin steel dots.

The common Additive Manufacturing L-PBF laser tracks are not visible in this particular material. The adopted island scan strategy is almost never identifiable. The typically laser scanning pattern is not evident. This is probably due to the fact that the non-interaction behavior of the two materials do not generate an homogeneous simmetric melting pool respect to the scanning direction while the laser vector melt the powder in a straight line of motion. A previous Sophia High Tech s.r.l. work concerning a Inconel718-Cu material shows a completely different XY microstructure:[4]

DOI: 10.13009/EUCASS2023-844

this is due to the fact that the material has at maximum a 20 % of copper and therefore the two different materials are able to create a Cu-Ni alloy. C. Tan at al.[20] show that an important inter-diffusion region at the boundary interface between 316L steel and copper exist and the metal matrix composite materials shows a conpenetrated bi-material matrix. Another similar work has been performed by S. Osipovich et al.[13] proposing an interesting study which goal was to analyse the gradient transition zone structure in a steel-copper sample produced by double wire-feed electron beam additive manufacturing: the transition zone is very similar to the microstructure observed in the present study. In particular a multi island area with different shapes, respect to the Copper concentration, is presented. They state that the composite structure shows a microstructure dominate by continuous interdendrite boundaries. The new Cu174PH6535 composite material seems to have a qualitative similar structure.

The Z build direction ZX or ZY plane of the material do not show obvious melting pools (Figure 10). Also the layer by layer stratification is not evident since the material is composite by two different alloys. A particular behavior of the composite material is the complex melting pool. The melting pool shape is concave respect to the Z building direction (face up curved). Randomly it is possible to identify that the basement of the melting pool are composed by copper or by the 17-4PH alloy (Figure 10(c)). A possible hypothesis for the copper based melting pool is that, since copper powders are smaller that steel one and since copper is slightly heavier that steel, during the melting process copper is encouraged by gravity and fluidity to go down and, therefore, steel floats above copper.

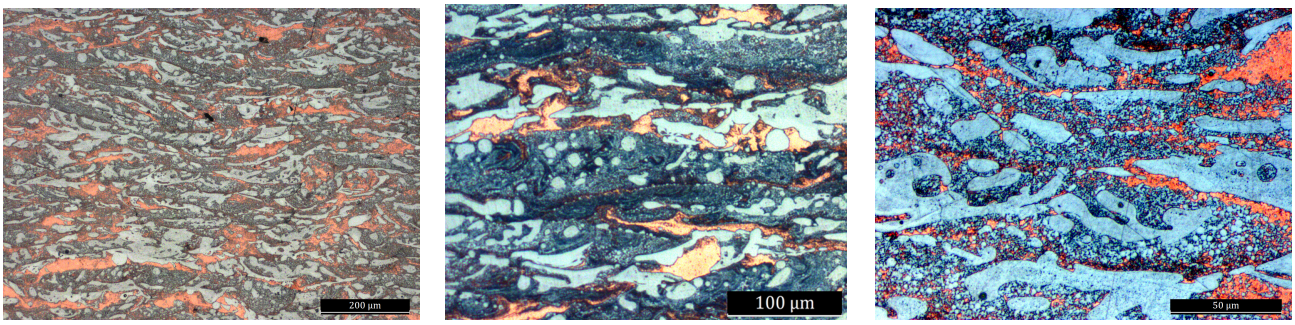

((a)) ((b)) ((c))

Figure 10: Cu174PH ZX/ZY plane micrography

3.2 Low Cycle Fatigue

The experimental results for low-cycle fatigue are presented in Table 3 and Figure 11(a). The effect of a main amplitude has not been investigated together with the effect of the strain rate. The latter is not trivial and negligible, as demonstrated by NASA studies for bulk copper alloys.[1] The effect of strain rate on the low-cycle fatigue behavior of the Narloy-z alloy at 538^{o}C was studied using strain rates of 4 x 10e-4 , 1 x 10e-2 and 5.2 x 10e-2 Hz. A comparison of these data indicates a clear increase in fatigue life as the strain rate increases.

It is possible to observe (Figure 11(a)) that at room and 150^oC temperatures there are no notable differences with respect to the slope of the curves. There is a qualitative linear proportion between room temperature and 150^oC tests: for a given strain amplitude life increases or decreases by a quasi-constant amount. On the other hand, at higher temperature, such as 350^oC and 550^oC the material behavior change: for 350^oC Cu174PH6535 shows a lower life at high strain amplitudes ad a higher life at lower amplitudes, respect to the 550^oC. A brief comparison with common historical and modern bulk NASA's copper alloys at different temperatures is presented in Figure 11(b).

A comparison of multiple stabilized (50% cycles to fracture) cycles for 3 different strain amplitudes for all temperatures tested is provided in Figure 12, for $\Delta\varepsilon$ = 2.0,$\Delta\varepsilon$ = 2.8 and $\Delta\varepsilon$ = 3.6, respectively. The $\Delta\varepsilon$ = 2.0 tests shows a remarkable difference between curves below the 550^oC and the one at 550^oC. On the other hand, when a $\Delta\varepsilon$ = 2.8 is applied, the temperature seems to less affect the hysteresis curve shape. However at 550^oC there still is a slightly breakdown and a overall bigger hysteresis curve. The higher $\Delta\varepsilon$ = 3.6 strain amplitude demonstrates, instead, that for very high strains the temperature does not affects the mechanical behavior of the Cu174PH6535 as was appending for lower amplitudes. In this particular case it is possible to state that the mechanical load is predominant respect to the temperature effects on the material's matrix.

The cyclic behaviour of the material subjected to increasing strain cycles can be represented by a cyclic curve which relates the amplitude of the total real strain cycle to the real stress variation for stabilised hysteresis cycles. The construction of the curve is based on the envelope of the vertices of the stabilised hysteresis cycles at various strain levels. The cyclic curve can be expressed with the Ramberg-Osgod model commonly employed for the monotonic tensile

DOI: 10.13009/EUCASS2023-844

Table 3: LCF high temperature and room temperatures Tests

			$\varepsilon_{eng}\%$		σ_{eng} [MPa]		$\sigma_{eng}[MPa]$ 50% cycles to failure			Repeatability	
	$\Delta\varepsilon eng.\%_{tot}$	Cycles to Fracture	Max	Min	Max	Min	Max	Min	Delta	Cycles to Fracture	Difference and Standard Deviation
T_room	0.5	**>6000**	0.25	-0.25	200	-131	184	-94	278		
	1.4	**>6000**	0.71	-0.70	346	-279	318	-269	588		
	2.0	**4180**	1.01	-1.00	422	-393	382	-384	767		
	2.8	**635**	1.41	-1.40	487	-470	460	-469	930		
	3.6	**136**	1.81	-1.80	530	-529	517	-520	1037		
T_150°C	2.0	**1447**	1.01	-1.00	369	-335	338	-334	672		
	2.8	**271**	1.41	-1.40	418	-403	394	-392	787		
	3.6	**63**	1.80	-1.80	446	-440	429	-413	842		
T_350°C	2.0	**795**	1.00	-1.00	287	-350	280	-283	564		
	2.8	**33**	1.41	-1.40	352	-342	339	-338	677		
	3.6	**14**	1.80	-1.79	362	-364	354	-350	704		
T_550°C	1.0	**1539**	0.50	-0.50	162	-164	160	-156	316		
	1.4	**546**	0.70	-0.70	183	-187	178	-184	362	**430**	21.24% - ST.DEV = 58
	2.0	**144**	1.00	-1.00	203	-210	200	-207	407		
	2.8	**39**	1.40	-1.40	250	-255	247	-252	499	**30**	23.07% - ST.DEV = 6.36
	3.6	**12**	1.81	-1.80	232	-229	231	-228	459		

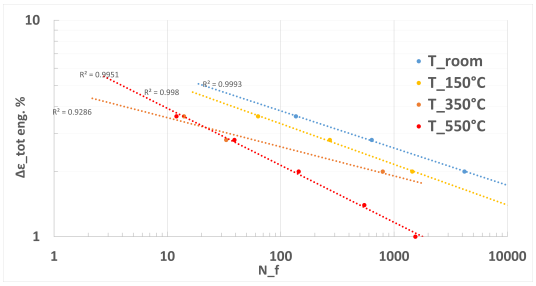

((a))

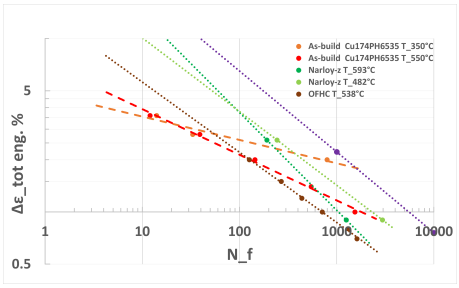

((b))

Figure 11: Low cycle fatigue cycle to failure representation. a) Low cycle fatigue experimental results. b) Cu174PH6535 and historical NASA's copper alloys life comparison, NASA's data from[1] and.[5]

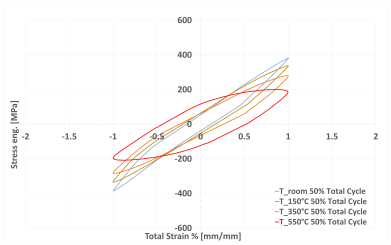

((a))

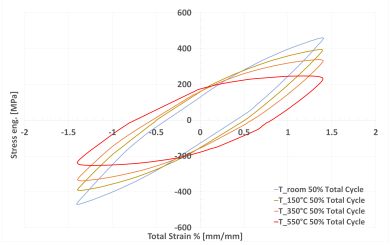

((b))

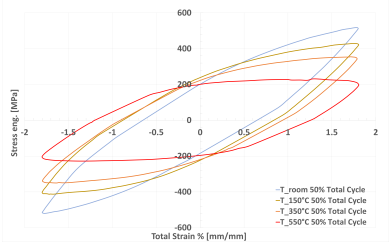

((c))

Figure 12: Low Cycle Fatigue temperature effect at constant strain. a) $\Delta\varepsilon_{tot}$ = 2.0% at 50% of total cycles vs Temperature. b) $\Delta\varepsilon_{tot}$ = 2.8% at 50% of total cycles vs Temperature. c) $\Delta\varepsilon_{tot}$ = 3.6% at 50% of total cycles vs Temperature.

curve. The only difference respect to the monotonic model is the exponent and coefficient of hardening are computed in order to fit the experimental cycling curve. Figure 13 shows the different cycling curves for high temperatures.

The R.-O. has been used for the cycling curve models and the results are presented in Figure 14. It is possible to observe that the model has a very high accuracy and it seems to be able to replicate the experimental real results. Therefore it is possible to state that the model can replicate the behaviour of the Cu174PH6535 bi-metallic composite material with excellent results. Table 4 present the exponent and the coefficient of cycling hardening at different temperatures.

Unixial damage models purposely designed to process experimental data from test campaigns on standard specimens can be used to estimate the low cycle fatigue life of materials. The goal is to discover a number of fatigue parameters for the material. Furthermore, the calibration of an uniaxial damage models is the starting point for multiaxial damage criteria, which allows complicated component fatigue life to be predicted.[11] The plastic strain component

DOI: 10.13009/EUCASS2023-844

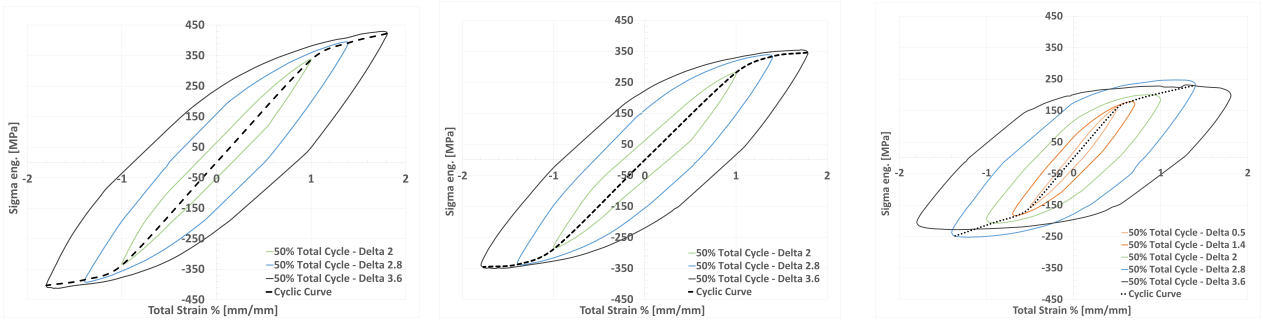

((a)) ((b)) ((c))

Figure 13: Low Cycle Fatigue strain effect at constant temperature and cycle curve. a) $\Delta\varepsilon_{tot}\%$ at 50% of total cycles at 150^{o}C. b)$\Delta\varepsilon_{tot}\%$ at 50% of total cycles at 350^{o}C. c) $\Delta\varepsilon_{tot}\%$ at 50% of total cycles at 550^{o}C.

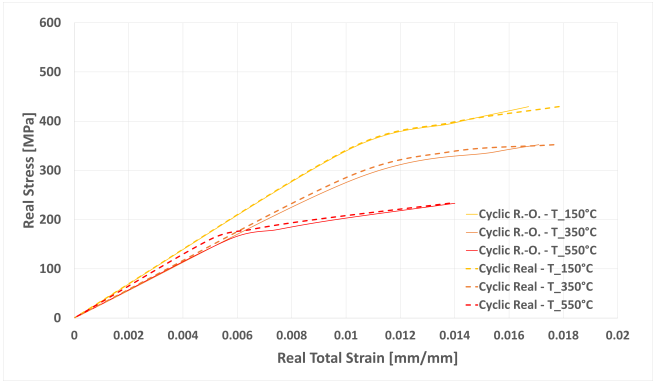

Figure 14: Ramberg - Osgood cycling curve comparison with real cycling curve

Table 4: Ramberg - Osgood Cycling curve relationship

Ramberg - Osgood Cycling curve relationship		
	K'	n'
Room	4265.79	0.48
150^{o}C	2187.76	0.37
350^{o}C	1737.8	0.37
550^{o}C	1122.01	0.35

has been thoroughly explored by two independent pioneering research on low cycle fatigue of ductile metals[?] carried out by Manson and Coffin in 1954. As a result, the Coffin-Manson model, which is an empirical model based on the strain-partitioning technique, has been successfully employed for the Cu174PH LCF unixial life.

The model shows that the fatigue life, in terms of number of cycles to fracture Nf, can be connected to the plastic strain range $\Delta\varepsilon_p\%$ by a simple exponential relationship, similar to the one already proposed by Basquin for High Cycle Fatigue, presented as follows:

$$\frac{\Delta\varepsilon}{2} = \varepsilon_f^{'} N_f^c \tag{1}$$

where, the fatigue ductility coefficient $\varepsilon_f^{'}$ and the exponent c are the material parameters.

Table 5 shows the calibrated Cu174PH6535 Coffin-Manson model parameters at different temperature. A log-log chart representation of the model results compared to the real experimental data (Figure 15).

The first room-temperature LCF test at $\Delta\varepsilon = 0.5$ shows a strong general hardening behavior. The max-min stress graph in Figure 16 shows a rising maximum stress and minimum respect to time (cycle number) increasing. The non-perfect linear shape of the curve, for both maximum and minimum plots, is probably due to the island structure of the material matrix. The presence of voids create a clear up and down curve shape. In particular when the local slop is positive the material is hardening (the stress in increasing) and therefore the rigidity of material is higher than

DOI: 10.13009/EUCASS2023-844

Table 5: Coffin-Manson equation Parameters

	$\varepsilon_f^{'}$	c
Room	8.31	-0.173
150^{o}C	7.76	-0.188
350^{o}C	4.78	-0.130
550^{o}C	6.76	-0.240

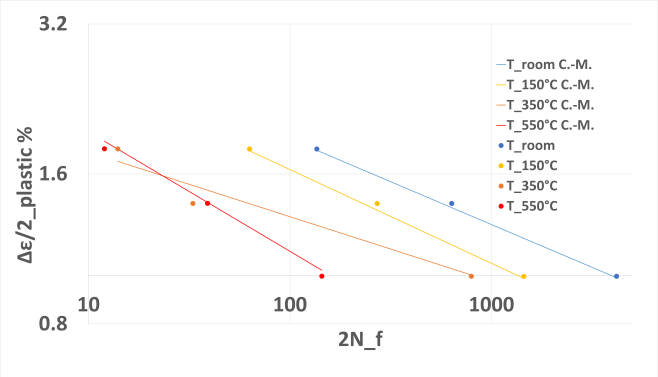

Figure 15: Low cycle fatigue Coffin-Manson model compareson with experimental data

the starting one (the more the material is stiff the more the behavior is hardening): this is probably due to the local voids coalescence and union. The more the voids collapse or combine the less available resistant area there is and therefore the materials try to reply with an hardening behavior. On the other hand when the local slop is negative the material is softening (the stress in decreasing) and therefore the rigidity of material is getting lower than the previous maximum of the hills. This is the a growing voids phase. Porosity are stretching on the axial traction direction without combine each other: the local resistant area do not change and therefore for the same required deformation the material is able to better strain with less stress. After the local softening phase is is possible to observe a little flat curve. However, after few cycle, voids (different shape, dimension and location) start a new coalescence: this phenomenon is repetitive and the experimental evidence of cycling local softening and hardening can be observed.This particular hypothetical phenomenon can be observed only for low deformation. This could be due to the fact that, probably, there is a characteristically time for activate the phenomenon. By observing the higher strain and higher temperature LCF tests this phenomenon does not show up; therefore, there is a potential threshold limit for the combination of strain and the temperature over which it is not possible to observe this phenomenon.

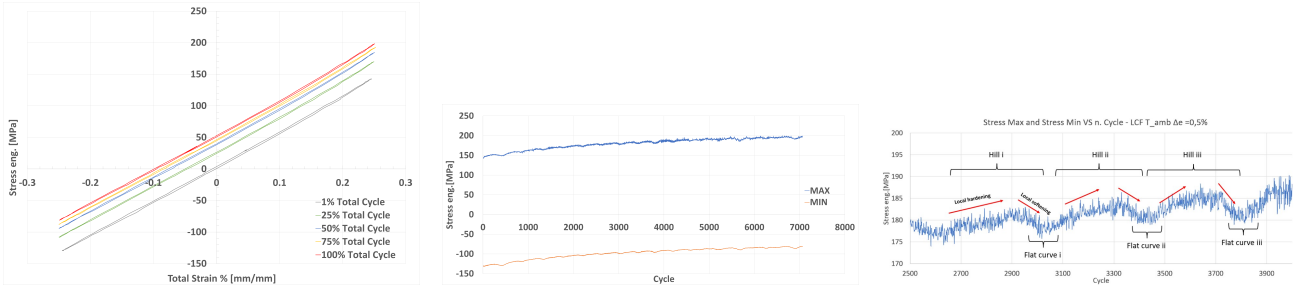

((a)) ((b)) ((c))

Figure 16: Room temperature LCF test at $\Delta\varepsilon = 0.5\%$. a) Cycles at different cycle to failure steps. b) Maximum and minimum stresses to failure. c) Local hardening and local softening effect.

Additionaly, a stress breakdown phenomenon exhibit at high temperatures and high strains. The maximum-minimum stresses plot of the LCF 350^oC test at $\Delta\varepsilon = 2.0$ (Figure 17) shows two particularities: i) a starting hardening behavior is present for several cycles (approximately 20 cycles); this attitude has already been observed in LCF Narloy-z NASA's bulk copper alloy;[1] ii) a double evident breakdown can be observed: the first stress failure occurred slightly after the 300th cycle and the second one around the 600th cycle (Figure 17(c)). Also the overall LCF test at 350^oC

DOI: 10.13009/EUCASS2023-844

is governed by a general softening behavior but, in contrast with the experimental evidence of room temperature and 150^oC LCF tests,in the middle of the maximum/minimum stress chart, no flat behavior is observed. The temperature raising is starting to governing the matrix behavior and it seems to have more influence with respect to the phenomenon of elongation and coalescence of voids.

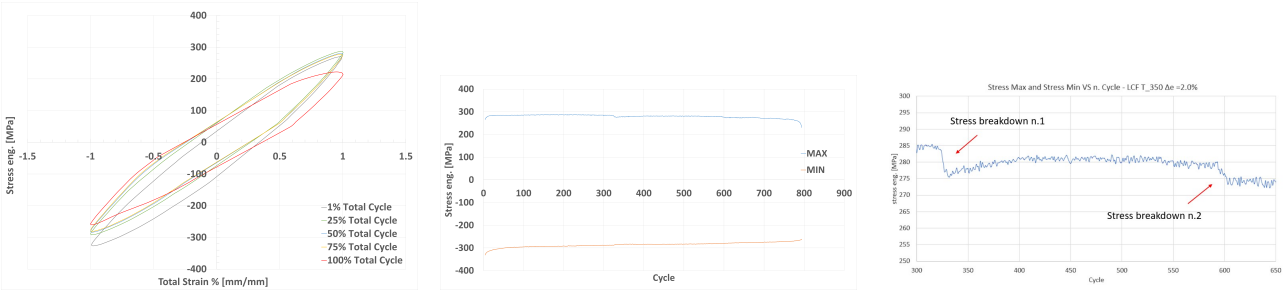

((a)) ((b)) ((c))

Figure 17: 350^oC temperature LCF test at $\Delta\varepsilon = 2.0\%$. a) Cycles at different cycle to failure steps. b) Maximum and minimum stresses to failure. c) Stress breakdown effect.

3.3 Creep

The result of the creep test shows a remarkable primary creep and a low rate secondary creep, as expected for a low elongation to fracture material, such as the under study Cu174PH6535. A logarithmic representation is provided in Figure 18(b). The secondary creep is clearly distinguishable from the primary phenomenon. The logarithmic time representation allows to observe the general behavior of the Cu174PH6535 respect to an instantaneous load: by monitoring the trasition from primary to secondary creep it is possible to observe that there is not a direct starting point for the secondary creep. After evident primary non-linear creep a hump is present and then a slight creep relaxation phenomenon comes up, thus the strain decreases with time. After this first decline phase and the local flat stabilization, the secondary creep phenomenon starts. This particular hump behavior is evident at 500^oC independently from the load range and it seems to be negligible for the lower 300^oC temperature.The strain rate $\dot{\varepsilon}$ has been evaluated with a linear regression respect to the more linear as possible largest time range. In particular all tree creep tests strain rates have been calculated in the range between 50000 [s] and 300000 [s], corresponding to a total 70 [h] range.

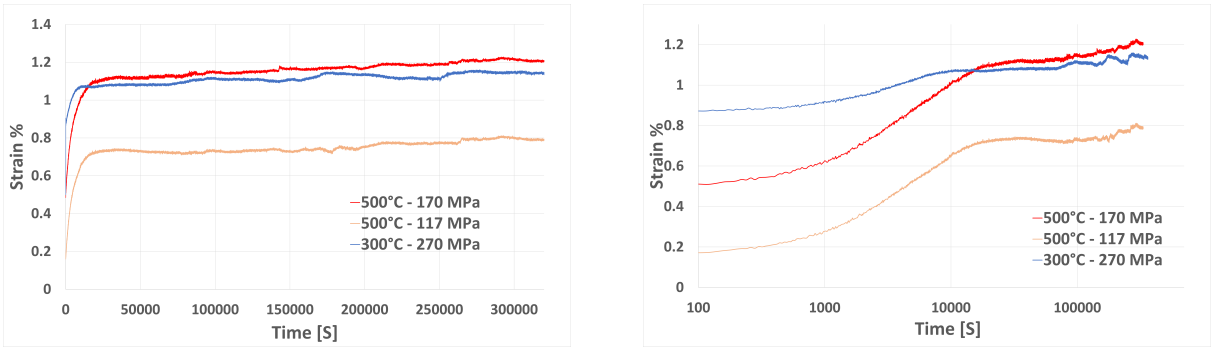

((a)) ((b))

Figure 18: Creep tests ad different stress levels and temperatures. a) Linear graph representation. b) Logarithmic graph representation.

The chart presented in Figure 19 shows the time-stress respect to strains rate behavior of the Cu174PH6535 composite, the modern bulk GRCop-84 and GRCop-42 NASA's copper alloys.[5] It is possible to observe that the Cu174PH6535 has a very low creep strain rate dependence respect to stress.

The Low cycle Fatigue tests have proved that after a precise amount of time the Cu174PH6535 composite shows a local hill phenomenon. During creep tests is is possible to observe a very similar behavior, thus there is an other addiction experimental evidence of the aforementioned hypothesis about the relation between the material matrix and porosities.

DOI: 10.13009/EUCASS2023-844

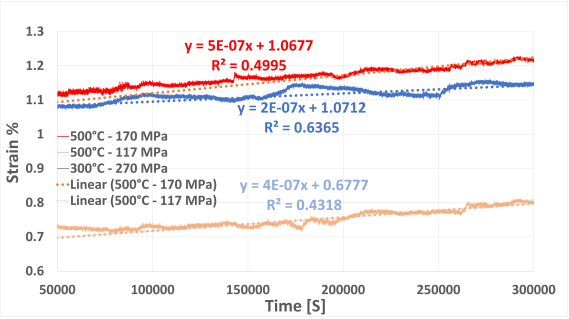

((a))

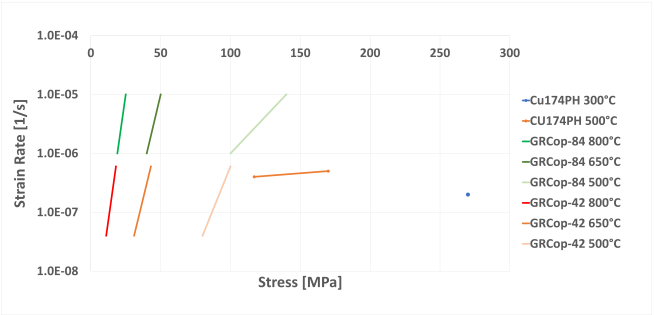

((b))

Figure 19: Creep strain rates. a) Cu174PH6535 creep strain rates at different temperatures and stress levels. b) Cu174PH6535 and modern bulk NASA's copper alloys Creep strain rates VS stress and temperature dependence.[5]

In particular, in Figure 20(a) it is possible to observe two main material breakdowns in both, 500^oC@117MPa and 300^oC@270MPa tests, thus the phenomenon do not seems to be highly dependent on stress and temperature loads. This phenomenon occurs approximately at the same time for all tree tests. The same behavior can be observed also in the 500^oC@170MPa creep test. Another remarkable fact that has been revealed by the observation of all creep test is that the multiple strain breakdown phenomenon requires a precise activation time (Figure 20(b)). Therefore before a qualitative amount of 2 hours there are no noticeable strain breakdowns. This 'breakdown limit' do not seems to be load of temperature highly dependent. The exactly same 'limit' behavior was found during the LCF tests, where before a certain number of LCF cycles none 'hill local phenomenon' was observed.

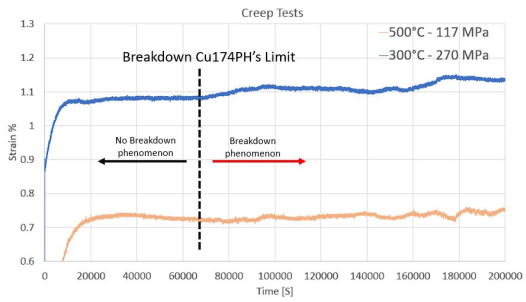

((a))

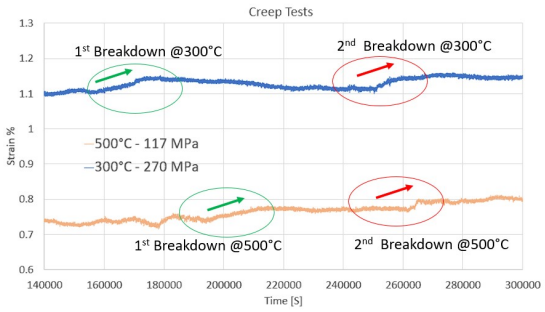

((b))

Figure 20: a) Cu174PH6535 breakdown limit. b) Cu174PH6535 breakdown phenomenon

3.4 Conclusion

The present work has been developed in order to explore an innovative Additive Manufacturing composite material Cu174PH6535 and study the feasibility to use it for future Liquid Rocket Engine application.

Low Cycle Fatigue (LCF) test at room and high temperatures have been successfully performed. Results show a general slight softening behavior, except for the 550^oC tests, where a more hardening effect can be clearly observed. The material behavior respect to cycling fatigue seems to be governed by the amplitude for room, 150^oC and 350^oC. The behavior at 550^oC seems to be less influenced by the high strain amplitude with respect to the rising of temperature itself. A particular stress breakdown time-activation phenomenon has been identified and named as 'local hill phenomenon'. The cycling curve model has been correctly employed in order to have an analytical model for cycling at different temperature. Finally, Coffin-Manson damage models has been correctly adopted for life prediction analysis. The overall LCF attitude of the under study material can be classified as interesting for future liquid rocket application. However, a process parameters optimization should be performed in order to achieve a better density. Finally, creep tests have been performed at different temperatures and stress levels. Also during the visco-plastic analysis the breakdown limit effect has been identified. The experimental results prove a very low creep-rate of the Cu174PH6535, as expected because of the island material matrix. This is an additional positive behavior for the aforementioned applications.

DOI: 10.13009/EUCASS2023-844

References

[1] J B Conway, R H Stentz, and J T Berling. High temperature, low-cycle fatigue of copper-base alloys in argon: Part i - preliminaryresults for 12 alloys at 1000 f (538 c). page 51, 1973.

[2] R. Cook and G. Coffey. Space Shuttle Orbiter engine main combustion chamber cooling and life. In *9th Propulsion Conference*, Las Vegas,NV,U.S.A., 1973.

[3] R T Cook, E E Fryk, and J F Newell. Ssme main combustion chamber life prediction. *National Astronaut and Space Administration Langley Research Center Library*, page 302, 1983.

[4] A. El Hassanin, A.T. Silvestri, F. Napolitano, F. Scherillo, A. Caraviello, D. Borrelli, and A. Astarita. Laser-powder bed fusion of pre-mixed Inconel718-Cu powders: An experimental study. *Journal of Manufacturing Processes*, 71:329–344, November 2021.

[5] Paul R. Gradl, Christopher S. Protz, Kenneth Cooper, David Ellis, Laura J. Evans, and Chance Garcia. GRCop-42 Development and Hot-fire Testing Using Additive Manufacturing Powder Bed Fusion for Channel-cooled Combustion Chambers. In *AIAA Propulsion and Energy 2019 Forum*, Indianapolis, IN, August 2019.

[6] Oskar J. Haidn. Advance rocket engines. *Advances on Propulsion Technology for High-Speed Aircraft Educational Notes RTO-EN-AVT-150*, 2008.

[7] Felix Hotte, Christoph v. Sethe, Torben Fiedler, Matthias C. Haupt, Oskar J. Haidn, and Michael Rohdenburg. Experimental lifetime study of regeneratively cooled rocket chamber walls. *International Journal of Fatigue*, September 2020.

[8] Jingchao Jiang and Yongsheng Ma. Path Planning Strategies to Optimize Accuracy, Quality, Build Time and Material Use in Additive Manufacturing: A Review. *Micromachines*, 11(7):633, June 2020.

[9] John M Kazaroff, Robert S Jankovsky, and Albert J Pavli. Hot fire test results of subscale tubular combustion chambers. *NASA Technical Paper 3222*, 1992.

[10] Yanjin Lu, Songquan Wu, Yiliang Gan, Tingting Huang, Chuanguang Yang, Lin Junjie, and Jinxin Lin. Study on the microstructure, mechanical property and residual stress of SLM Inconel-718 alloy manufactured by differing island scanning strategy. *Optics & Laser Technology*, 75:197–206, December 2015.

[11] S. S. Manson. Thermal stress and low cycle fatigue. *Book*, 1996.

[12] Tadashi Masuoka and JÃ¶rg R Riccius. Life evaluation of a combustion chamber by thermomechanical fatigue panel tests based on a creep fatigue and ductile damage model. *International Journal of Damage Mechanics*, 29(2):226–245, February 2020.

[13] Kseniya S. Osipovich, Elena G. Astafurova, Andrey V. Chumaevskii, Kirill N. Kalashnikov, Sergey V. Astafurov, Galina G. Maier, Evgenii V. Melnikov, Valentina A. Moskvina, Marina Yu. Panchenko, Sergey Yu. Tarasov, Valery E. Rubtsov, and Evgeny A. Kolubaev. Gradient transition zone structure in 'steel-copper' sample produced by double wire-feed electron beam additive manufacturing. *Journal of Materials Science*, 55(22):9258–9272, August 2020.

[14] Albert J Pavli, John M Kazaroff, and Robert S Jankovsky. Hot fire fatigue testing results for the compliant combustion chamber. *NASA Technical Paper 3223*, page 13, 1992.

[15] Marco Pizzarelli. An Algebraic Model for Structural and Life Analysis of Regeneratively-Cooled Thrust Chambers. *Journal of Propulsion and Power*, 36(2):191–201, March 2020.

[16] R.J. Quentmeyer. Experimental Fatigue Life Investigation of Cylindrical Thrust Chambers. *AIAA/SAE 13th Propulsion Conference*, 1977.

[17] Joerg R. Riccius, Wissam Bouajila, and Evgeny B. Zametaev. Comparison of Finite Element analysis and experimental results of a combustion chamber type TMF panel test. In *49th AIAA/ASME/SAE/ASEE Joint Propulsion Conference*, San Jose, CA, July 2013. American Institute of Aeronautics and Astronautics.

[18] Alessandro Salmi, Flaviana Calignano, Manuela Galati, and Eleonora Atzeni. An integrated design methodology for components produced by laser powder bed fusion (L-PBF) process. *Virtual and Physical Prototyping*, 13(3):191–202, July 2018.

DOI: 10.13009/EUCASS2023-844

[19] Xiaosi Sun, Weixin Hao, Guihong Geng, Teng Ma, and Yongtang Li. Solidification Microstructure Evolution of Undercooled Cu-15 wt.% Fe Alloy Melt. *Advances in Materials Science and Engineering*, 2018:1–6, July 2018.

[20] Chaolin Tan, Youxiang Chew, Guijun Bi, Di Wang, Wenyou Ma, Yongqiang Yang, and Kesong Zhou. Additive manufacturing of steel-copper functionally graded material with ultrahigh bonding strength. *Journal of Materials Science & Technology*, 72:217–222, May 2021.

[21] R. G. Thiede, J. R. Riccius, and S. Reese. Life Prediction of Rocket Combustion-Chamber-Type Thermomechanical Fatigue Panels. *Journal of Propulsion and Power*, 33(6):1529–1542, November 2017.